

Why Static Friction Decreases From Single to Multi-asperity Contacts

Liang Peng^{1*}, Thibault Roch^{1*}, Daniel Bonn¹, and Bart Weber^{1,2}

¹ *Van der Waals-Zeeman Institute, Institute of Physics, University of Amsterdam, Science Park 904, 1098 XH Amsterdam, The Netherlands*

² *Advanced Research Center for Nanolithography (ARCNL), Science Park 106, 1098 XG Amsterdam, The Netherlands*

The key parameter for describing frictional strength at the onset of sliding is the static friction coefficient. Yet, how the static friction coefficient at the macroscale emerges from contacting asperities at the microscale is still an open problem. Here, we present friction experiments in which the normal load was varied over more than three orders of magnitude, so that a transition from a single asperity contact at low loads to multi-asperity contacts at high loads was achieved. We find a remarkable drop in static friction coefficient with increasing normal load. Using a simple stick-slip transition model we identify the presence of pre-sliding and subcritical contact points as the cause of smaller static friction coefficient at increased normal loads. Our measurements and model bridge the gap between friction behavior commonly observed in atomic force microscopy (AFM) experiments at microscopic forces, and industrially relevant multi-asperity contact interfaces loaded with macroscopic forces.

The onset of sliding is of critical importance to various natural and industrial interfaces. For example, stick-slip friction behavior leads to catastrophic energy release in earthquakes [1–4] and can hamper the functioning of microelectromechanical systems (MEMS) [5–7]. When slip is initiated, the static friction force generically reduces to a (lower) dynamic friction force [8–10]. This transition from static to dynamic friction, also known as friction drop, can be effectively described by the empirical rate and state friction (RSF) laws across various contact length scales [11–14]. However, the underlying physical mechanisms remain elusive.

Atomic force microscopy (AFM) friction experiments [15–18] and theoretical models [19–22] have shown that at silicon/silicon contacts, the dynamics of the formation and rupture of interfacial bond networks control the evolution of friction during the onset of slip. While recent experiments suggest that similar bonding phenomena also occur at larger multi-contact interfaces [23], additional complexity may emerge as contacts grow [11]. Examples of such complexity include the wear [24], multi-scale roughness [25], the widening of interfacial pressure distribution [26], nonconcurrent slip across the interface [27–29] and interactions between neighboring contact asperities [30, 31]. Systematic studies into how such complexity emerges as contacts grow are challenging because rough macroscopic contact interfaces consist of a myriad of contact asperities that are hidden from view by the bulk contacting bodies [32–34].

In this Letter, we experimentally demonstrate that the static friction coefficient decreases as the interface grows from single contact to multi-asperity contact by increasing the normal load applied to a silicon-on-silicon contact. The observed decreasing trend of static friction coefficient with increasing normal load can be captured by a simple stick-slip transition model, analogous to a fiber bundle model, based on the local normal contact stress map obtained from boundary integral contact calculations without adjustable parameters. We find that

three types of contact points can be identified when the interface is subjected to the maximal tangential force it can withstand. We describe these three types of contact asperities as “critical”, “pre-sliding” and “subcritical”. While single-asperity interfaces are always critical at the onset of slip, we show that the emergence of pre-sliding and subcritical contact asperities at multi-asperity interfaces causes the static friction coefficient to decrease.

We study silicon-on-silicon friction using a rheometer (DSR 502, Anton Paar) in combination with an analytical balance (Quintix, Sartorius) inside a humidity-controlled chamber, as shown in Fig. 1(a). Before the friction experiments, the (naturally oxidized) silicon balls (Goodfellow) were sonicated in ethanol and then Milli-Q water, followed by nitrogen flow drying. To compare with the highly hydroxylated silicon surfaces used in previous AFM experiments [15, 16], the silicon balls and the silicon cantilevers were then treated by oxygen plasma cleaning inside a reactor (Zepto One, Diener Electronic) [23]. In the friction experiments, both the plasma-cleaned silicon ball and the plasma-cleaned silicon cantilever were initially equilibrated for one hour inside the dry chamber before contact was formed between them. The relative humidity inside the chamber was stabilized at 0.8% by continuously flowing dry nitrogen. During the sliding, the rheometer and the balance simultaneously measured the friction force and normal load at the contact interface, respectively. By using silicon cantilevers of different normal stiffness, the normal loads were precisely varied from 0.1 to 100 mN. The imposed sliding speed was fixed at 0.3 $\mu\text{m/s}$ for all the measurements. A slide-hold-slide (SHS) measurement procedure was employed (see Fig. 1(b)): we imposed a stationary state with the rheometer after the initial sliding state, followed by reinitiating the sliding in the same direction. The static friction force (F_S) and dynamic friction force (F_D) when sliding was restarted, were recorded to calculate the corresponding static friction coefficient, μ_S , the dynamic friction coefficient, μ_D , and the normal-

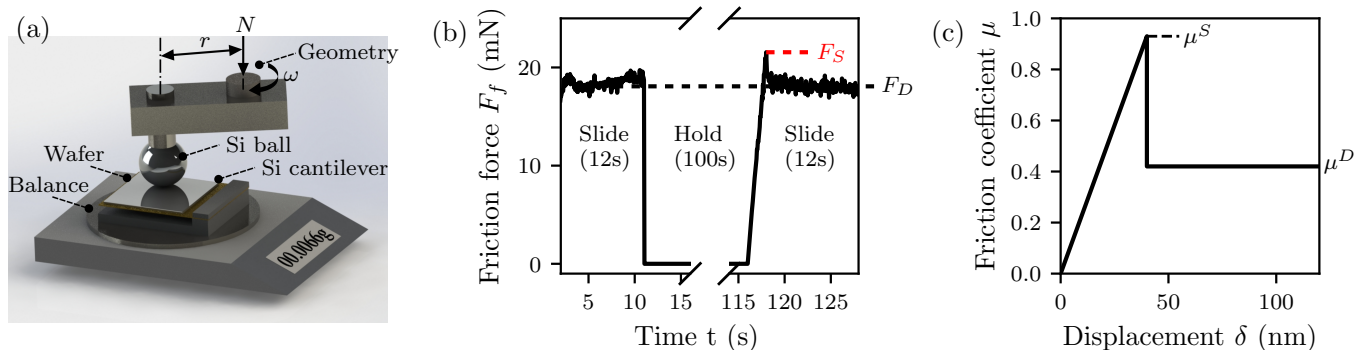


FIG. 1. Experimental system. (a) A 3 mm-diameter silicon ball inside a humidity-controlled chamber is clamped to the geometry of a rheometer and brought into contact with a homemade Si cantilever that is made by gluing a piece of 1×1 cm p-type silicon (100) wafer (University Wafer) to a brass sheet. The normal stiffness of the Si cantilever can be tuned by changing the width and thickness of the used brass sheet. The Si cantilever is mounted on a stage, which was attached to the weighing pan of an analytical balance by dead weight. By rotating the geometry at a constant angular velocity, ω , a sliding speed of ωr ($r = 10$ mm) is imposed at the Si-on-Si contact interface. The corresponding friction force (F_f) and the normal force (N) can be simultaneously measured by the rheometer and the balance. The ratio of friction force and normal load gives the coefficient of friction, $\mu = F_f/N$. (b) An example of the slide-hold-slide experiments protocol with a normal load of 24 mN and a hold time of 100 s. F_S and F_D represent the maximum static friction force and the average dynamic friction force after the sliding is reinitiated, respectively. (c) Reproduction of the nanoscale friction coefficient evolution with imposed displacement, from previous AFM experiments [15].

ized static friction coefficient (also called friction drop), μ_S/μ_D , which equals to F_S/F_D . All sliding strokes were measured on previously untouched areas of the silicon wafer and were kept short at 10 μm to minimize the influence of wear (Fig. S3).

Both the static and the dynamic friction coefficients, defined as the ratio of friction force to normal force, are widely assumed to be independent of the normal load [35–37]. Surprisingly, we observe that the static friction coefficient gradually decreases with increasing normal load as shown with black data points in Fig. 2, indicating a smaller friction coefficient at higher normal loads. Notably, the single-asperity nanoscale static friction (left-most black circle in Fig. 2), measured from previous AFM experiments (reproduced in Fig. 1(c)) [15], aligns well with our observed qualitative decreasing trend of friction drop with increasing normal load.

To provide insight into the normal load dependence of the friction drop, we propose a simple stick-slip transition model. In the model, we assume that the macroscopic friction force is the sum of all the microscopic interfacial shear forces generated by single asperity contacts. We also assume that the asperity-scale frictional behavior is characterized by an instant drop in friction upon slip, the magnitude of which matches that observed in the AFM friction experiments shown in Fig. 1(c). In other words, the local ratio of shear stress to normal stress drops at the onset of local slip, in accordance with the static and dynamic friction coefficient (μ^S and μ^D , respectively) observed in the AFM experiments (Fig. 1(c)). The applied shear force is assumed to be distributed homogeneously over all the contact asperities before any asperity starts to slip. The excess friction force that is generated when

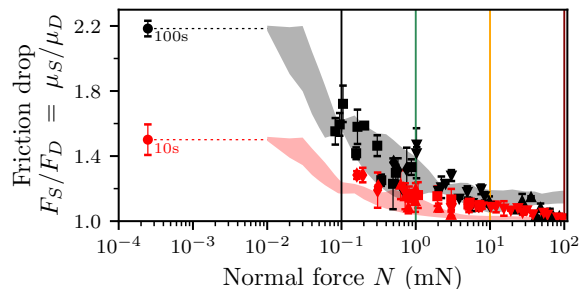


FIG. 2. The ratio of the static friction force to the dynamic friction force (also known as friction drop) as a function of normal load. The black and red data points correspond to a hold time of 100 s and 10 s, respectively. Different symbols represent the measurements using Si cantilevers of different normal stiffness and each data point represents the average of three measurements. The leftmost red and black solid circle data points, measured from AFM experiments, are extracted from Fig. S5 in Ref. [15]. The shaded area shows the friction drop calculated from our model using three different surface topographies (shown in Fig. S1) of the experimentally used Si balls, with red and gray indicating the result of a hold time of 100 s and 10 s, respectively. The vertical lines indicate the normal load corresponding to the normal stress distribution shown in Fig. 3.

a local contact asperity enters slip, is uniformly redistributed over all the contact asperities at the interface that have not undergone slip yet.

To estimate the local normal stress at the interface, we conduct elastic contact calculations using an open-source implementation of the boundary integral method (BIM)

[38]. The inputs for our contact calculations include the normal load, the silicon surface topography measured using AFM after friction experiments, and the mechanical properties of silicon: Young's modulus: $E = 130 \pm 3$ GPa, Poisson's ratio: $\nu = 0.26$. Our use of elastic contact is reasonable here, since there is mainly elastic deformation at the contact interface (see Fig. 3) [23, 30, 39]. Using the calculated local normal stress distribution and the assumed relations between local shear stress and local normal stress described above, the model predicts how the total friction force, which is externally imposed, is distributed over the contact points and how this distribution of local shear force evolves as the applied macroscopic tangential force is increased. As the local friction coefficient at each asperity is assumed to be uniform, it is the normal stress distribution that completely determines the frictional behavior. This enables us to predict the frictional response of the same interface at various normal loads, from which we can compute the static friction coefficient and friction drop.

In other words, our model is analogous to a fiber bundle model with equal load sharing [40], where the failure of a bundle of fibers corresponds to the failure of contact asperities, with their strength governed by the local normal stress. While sliding heterogeneity can originate from elastic interaction among contact asperities [11], we assume that these interactions among asperities during the onset of the sliding process are negligible in our system. Indeed, the interfacial nanometer-sized contact deformation (~ 5 nm at a normal load of 10 mN based on BIM contact calculation as mentioned above) is considerably smaller in comparison to the micrometer-scale distance between contact asperities, which supports our assumption of equal load sharing.

To quantify ball-to-ball topography variations, we use three different topographies extracted from silicon balls that were used in the experiments (see Fig. S1). For each topography and normal load, the model predicts the friction drop. The gray shaded area in Fig. 2 corresponds to the range of predicted friction drop values based on the three topographies, with the nanoscale static and dynamic friction coefficients measured at a hold time of 100 s in AFM experiments. The stick-slip transition model qualitatively reproduces the decrease of the friction drop with increasing normal load and quantitatively matches the experiments without any fitting parameter.

To evaluate the robustness of our model against variations in the system characteristics, we conduct additional experiments with a hold time of 10 s instead of 100 s, and report the corresponding friction drop with red data points in Fig. 2. A decrease of the friction drop with increasing normal load is observed, similar to the experiments for a hold time of 100 s. Furthermore, it is noteworthy that the measured friction drop for a hold time of 100 s is larger than that for a hold time of 10 s under the same normal force. The larger static friction coefficient, corresponding to a greater friction drop, is expected: a longer hold time during the SHS procedure can enhance

the contact strength by forming more interfacial siloxane bonds [15, 23], which results in a higher static friction coefficient. Moreover, our stick-slip transition model (red-shaded area in Fig. 2) with the nanoscale static and dynamic friction coefficients measured at a hold time of 10 s from previous AFM experiments [15] (leftmost red circle in Fig. 2, see also Fig. S2), still captures successfully the evolution of friction drop with the normal force for the experiments with 10 s hold time.

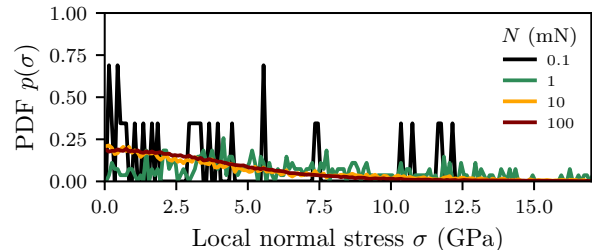


FIG. 3. The probability density function, $p(\sigma)$, of the local normal stress σ under various normal loads.

One should note that there is still a gap between the minimum normal load used in the simulation and AFM experiments in Fig. 2 (marked by black and red horizontal dot lines), which will be discussed later.

To further elucidate the relation between the normal load, the local normal stress distribution, and the macroscopic frictional response, we plot the probability density function, $p(\sigma)$, of the normal stress at the interface, obtained from elastic contact calculations with various normal loads in Fig. 3. With increasing normal load, the probability density function of the local normal stress evolves from being discrete (the black curve, 0.1 mN) to continuous (the yellow curve, 10mN). This directly relates to the transition from single to multi-asperity contact interfaces. At lowest normal loads, only a few contacts are formed, and the macroscopic behavior may be dominated by those asperities. At largest normal loads, however, there is a more continuous distribution of normal (and thus shear) stresses at the interface. The normal loads corresponding to the distribution shown in Fig. 3 are indicated with vertical lines of the same color in Fig. 2.

To better understand how the differences in normal stress distribution impact the onset of sliding, we focus on the critical state of the interface, where the peak macroscopic friction coefficient is reached under an imposed tangential force corresponding to an imposed lateral displacement of δ_{peak} , see a typical friction versus displacement curve from a numerical simulation in Fig. 4(a). We plot the distribution of local friction coefficients across all the contact asperities at the critical state of the interface in Fig. 4(b)-(e). For a single asperity contact (Fig. 4(b)), the asperity will reach the local maximum static friction coefficient, μ^S , resulting in an interfacial friction coefficient equal to the local friction coefficient ($\mu = \mu^S$). In

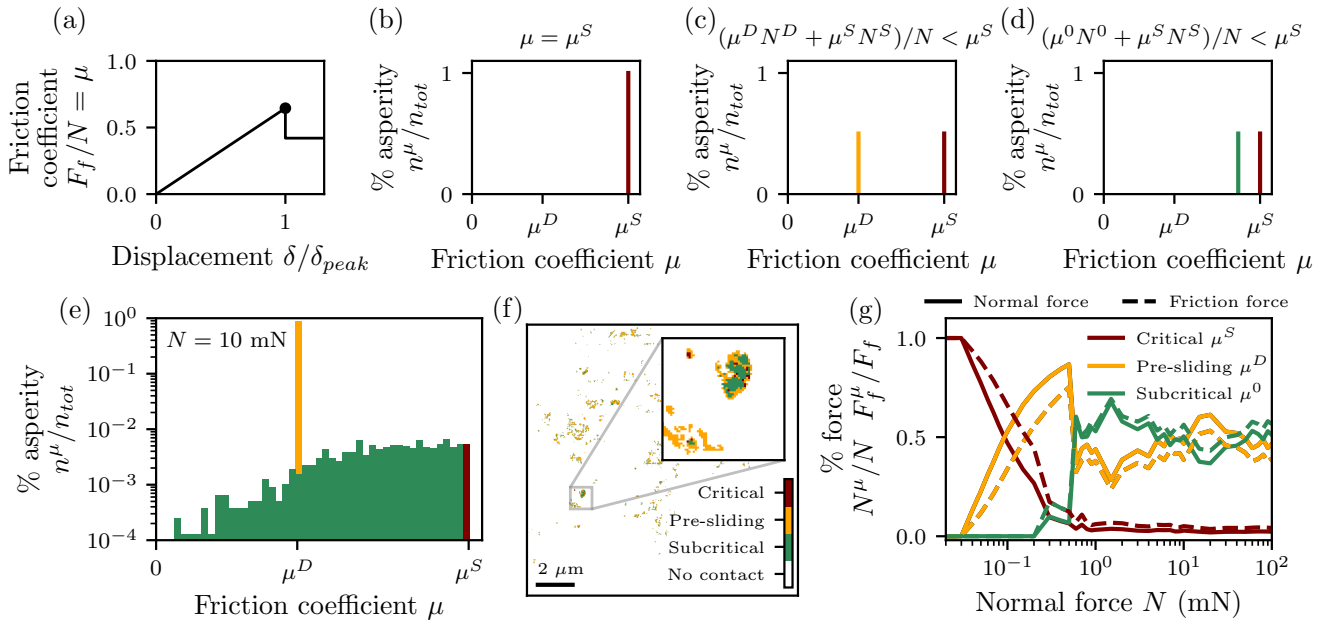


FIG. 4. Local stick-slip transition at the critical state of the interface from numerical computation. (a) Friction coefficient vs displacement curve for the interface at a normal load of 0.1 mN. The black circle corresponds to the critical interfacial state where no more additional tangential load can be added. (b) to (e) Distribution of local friction coefficient for a single-asperity interface (b), two-asperity interface (c)(d), and multi-asperity interface under a normal load of 10 mN (e), respectively. The brown, yellow, and green correspond to the critical, pre-sliding, and subcritical asperities with local friction coefficients of μ^D , μ^S , and μ^0 , respectively. μ^0 is smaller than μ^S . n^μ and n^{tot} represent the number of asperities under a local friction coefficient of μ ($\mu = \mu^S, \mu^D$, or μ^0) and the total number of asperities, respectively. Movies of the evolution of the distribution of local friction coefficient with increasing imposed displacement are available [online](#) (f) The state of the contacting asperities at the critical interfacial state for a normal load of 10 mN. (g) The fraction of the total normal force (solid lines) and the total friction force (dashed lines) generated by different types of contact asperities in the interfaces under various normal loads. N^μ and N represent the shared normal load on those contact asperities under a local friction coefficient of μ ($\mu = \mu^S, \mu^D$, or μ^0) and the total applied normal load, respectively. F_f^μ and F_f represent the same quantity but for the shear load.

this limiting case of a single asperity contact, one recovers the frictional behavior as measured from AFM. In our model, this means that below a normal load for which the real contact area is of the scale of the input AFM topography resolution (21 nm), the macroscopic friction coefficient is not dependent on the normal load. Such an extreme case is marked by black and red horizontal dot lines in Fig. 2.

The situation becomes more complex when considering multi-asperity contact interfaces, as each asperity potentially experiences different local normal forces (and thus different local friction coefficients at the critical interfacial state). We stress that, within our model, any distribution of local friction coefficients (between 0 and μ^S) at a multi-contact interface can only result in a decrease in the macroscopic static friction coefficient as compared to the maximum static friction coefficient (μ^S) at single-asperity level (Fig. 4(b)). Hereafter we investigate the details of the critical interfacial state for multi-asperity interfaces and its influence on the macroscopic friction coefficient, starting with two contacting asperities.

For an interface composed of two contacting asperities, each carrying a different normal force, two distinct sce-

narios arise at the critical interfacial state corresponding to maximal static friction force. In the first scenario, the normal force carried by each asperity varies significantly (Fig. 4(c)) such that the weaker asperity, carrying a smaller normal force, has already slipped and experiences local friction coefficient μ^D , while the stronger asperity with the higher normal force remains stuck with a local friction coefficient of μ^S . We can then calculate the interfacial friction coefficient as $\mu = (\mu^D N^D + \mu^S N^S)/N$, where N^D and N^S represent the normal force carried by the two asperities: $N = N^D + N^S$. The corresponding local friction coefficients are μ^D and μ^S , respectively. In the second scenario, the difference in the normal forces carried by the two asperities is smaller (Fig. 4(d)). This results in both contact asperities being stuck at the critical state of the interface. Now, the failure of the weaker asperity will trigger the slip of the stronger asperity due to its excess friction force redistribution. The asperity with lower normal force has reached a coefficient of μ^S , while the contact asperity with higher normal force experiences a local friction coefficient of μ^0 that is smaller than μ^S . Note that contrarily to μ^D and μ^S , μ^0 is not a fixed value related to the nanoscale fric-

tion experiment: it is the instantaneous friction coefficient experienced by a stuck asperity that is loaded subcritically. The calculated interfacial friction coefficient is then $\mu = (\mu^0 N^0 + \mu^S N^S)/N$, where N^0 and N^S represent the normal force on the two asperities, satisfying $N = N^0 + N^S$ and $N^0 > N^S$. In both scenarios the static friction coefficient is lowered by the addition of a second asperity, either because an asperity has already entered slip when the overall friction force is maximal (scenario 1) or because the stronger asperity is “subcritical”; its slip is activated by failure of the weaker asperity (scenario 2).

We can therefore define three types of contact asperities at the critical state of multi-asperity interfaces: critical contact asperities, defined as those that experience the local static friction coefficient of μ^S ; pre-sliding contact asperities, defined as those that have already slipped and therefore show the dynamic friction coefficient of μ^D ; and subcritical contact asperities, defined as those with a local friction coefficient of μ^0 that is smaller than μ^S . For a realistic multi-asperity interface, many asperities might correspond to each of the three asperity types. An example is shown in Fig. 4(e), with the distribution of local friction coefficients for an interface at the critical state under a normal load of 10 mN. The three types of asperities (critical, pre-sliding, and subcritical) are respectively represented in green, yellow, and brown. The corresponding contact map from the BIM computation is shown in Fig. 4(f), with the contact being colored following the same scheme.

The slip of the subcritical asperities is activated by redistribution of excess friction force released when the critical asperities slip. This instability in our model defines the critical interface state with maximal applied tangential load. Since both μ^D and μ^0 are smaller than μ^S , the interfacial friction coefficient at the critical interfacial state will, as expected, be smaller as compared to that in a single asperity interface ($\mu < \mu^S$). Consequently, it is the pre-sliding and subcritical contact asperities that dominate the reduction of the macroscopic static friction coefficient at the multi-asperity interfaces with respect to its value for a single asperity interface, leading to a smaller friction drop with increasing normal load. In other words, the critical asperities govern the maximum static friction coefficient. To quantify the relative contribution of critical, pre-sliding, and subcritical contact asperities to the overall static friction coefficient, we plot the fraction of the total normal load (respectively friction force) supported by different types of contact asperities under various total normal loads in solid (respectively dashed) lines in Fig. 4(g). As the total normal load increases, more contact asperities form at the contact interface. The fraction of pre-sliding and subcritical contact asperities gradually increases from 0 at single asperity contact interface to an approximately constant value at multi-asperity contact interface, which suggests a greater reduction of static friction coefficient and thus results in a smaller macroscopic static friction coefficient. In con-

trast, the fraction of critical contact asperities decreases from 1 to an almost negligible level. This decreasing fraction of critical contact asperities with increasing normal load indicates a smaller contribution of critical contact asperities to the static friction coefficient, which matches well with the observed friction drop in Fig. 2. We expect the range of load over which the fraction of critical asperities is replaced by pre-sliding and subcritical asperities to depend on the bulk parameters and the geometric details of the surfaces, for example, their roughness.

In conclusion, we have investigated how the macroscopic frictional response of a Si-on-Si system evolves from a single to a multi-asperity contact interface, and shown how the macroscopic static friction coefficient decreases with increasing normal load across a broad range of loads. We propose a stick-slip model, analogous to a fiber bundle model, based on elastic contact calculations to capture the decrease in macroscopic static friction coefficient and friction drop with increasing normal load. This decrease is found to be dominated by the relative fraction of critical contact asperities at the interface that collectively fail when the maximal static friction force is reached. With increasing normal load, we observe the growing populations of pre-sliding asperities - contact asperities that slip before the maximal tangential force is applied to the interface- and subcritical asperities - contact asperities whose slip is activated by redistribution of the excess friction from critical asperities. Both the pre-sliding and subcritical populations of asperities observed at the critical interface state grow with increasing normal load, causing the static friction coefficient to drop with increased normal force. By changing the hold time in our hold-slid-hold experiments, we demonstrated that these results remain valid when considering a different reference nano-scale friction behavior. While our experiments were limited to Si-on-Si interface, we believe our results to be relevant for the transition from single to multi-asperity contact of generic interfaces, for which the elastic interactions between contact asperities remain negligible. We expect the range of normal load over which the decrease in macroscopic friction occurs to be dependent on both the material properties and the details of the surface (e.g., its roughness), an issue that should be addressed in future work. All in all, our findings shed new light on the complexity that emerges when contact interfaces scale up from single asperity to multi-asperity - a central question in tribology and an important challenge in precision positioning.

ACKNOWLEDGMENTS

We thank R. Carpick, B. Mcclimon, J. Dijksman and K. Farain for valuable discussions. TR acknowledges support of the Swiss National Science Foundation through the fellowship No. P500PT/222342. LP thanks the invaluable support from Min Li.

* L. Peng and T. Roch contributed equally.

- [1] A. Ruina, Slip instability and state variable friction laws, *Journal of Geophysical Research: Solid Earth* **88**, 10359 (1983).
- [2] C. H. Scholz, Earthquakes and friction laws, *Nature* **391**, 37 (1998).
- [3] M. J. Ikari, C. Marone, D. M. Saffer, and A. J. Kopf, Slip weakening as a mechanism for slow earthquakes, *Nature Geoscience* **6**, 468 (2013).
- [4] K. Farain and D. Bonn, Perturbation-induced granular fluidization as a model for remote earthquake triggering, *Science Advances* **10**, 1 (2024).
- [5] A. Corwin and M. De Boer, Effect of adhesion on dynamic and static friction in surface micromachining, *Applied Physics Letters* **84**, 2451 (2004).
- [6] B. Weber, J. Scheibert, M. De Boer, and A. Dhinojwala, Experimental insights into adhesion and friction between nominally dry rough surfaces, *MRS Bulletin* **47**, 1 (2022).
- [7] S. S. Shroff, N. Ansari, W. Robert Ashurst, and M. P. de Boer, Rate-state friction in microelectromechanical systems interfaces: Experiment and theory, *Journal of Applied Physics* **116** (2014).
- [8] B. Weber, T. Suhina, A. Brouwer, and D. Bonn, Frictional weakening of slip interfaces, *Science Advances* **5**, 1 (2019).
- [9] T. Baumberger and C. Caroli, Solid friction from stick-slip down to pinning and aging, *Advances in Physics* **55**, 279 (2006).
- [10] C. Mate and R. Carpick, *Tribology on the Small Scale: A Modern Textbook on Friction, Lubrication, and Wear* (Oxford University Press, 2019).
- [11] S. Li, S. Zhang, Z. Chen, X. Feng, and Q. Li, Length scale effect in frictional aging of silica contacts, *Physical Review Letters* **125**, 215502 (2020).
- [12] K. Tian, Z. Li, N. Gosvami, D. Goldsby, I. Szlufarska, and R. Carpick, Memory distance for interfacial chemical bond-induced friction at the nanoscale, *ACS Nano* **13**, 7425 (2019).
- [13] L. Frérot, A. Crespo, J. El-Awady, M. Robbins, J. Cayer-Barrioz, and D. Mazuyer, From molecular to multi-asperity contacts: how roughness bridges the friction scale gap, *ACS Nano* 10.1021/acs.nano.2c08435 (2021).
- [14] R. Sahli, G. Pallares, C. Ducottet, I. Ben Ali, S. Al Akhrass, M. Guibert, *et al.*, Evolution of real contact area under shear and the value of static friction of soft materials, *Proceedings of the National Academy of Sciences* **115**, 471 (2018).
- [15] Q. Li, T. Tullis, D. Goldsby, and R. Carpick, Frictional ageing from interfacial bonding and the origins of rate and state friction, *Nature* **480**, 233 (2011).
- [16] K. Tian, N. Gosvami, D. Goldsby, Y. Liu, I. Szlufarska, and R. Carpick, Load and time dependence of interfacial chemical bond-induced friction at the nanoscale, *Physical Review Letters* **118**, 1 (2017).
- [17] M. Vorholzer, J. Vilhena, R. Perez, E. Gnecco, D. Dietzel, and A. Schirmeisen, Temperature activates contact aging in silica nanocontacts, *Physical Review X* **9**, 1 (2019).
- [18] N. Badt, D. Goldsby, G. Pharr, and C. Walker, Frictional aging of single-asperity nanoindentation contacts in quartz and calcite, *Geophysical Research Letters* 10.1029/2023GL105471 (2024).
- [19] W. Ouyang, S. Ramakrishna, A. Rossi, M. Urbakh, N. Spencer, and A. Arcifa, Load and velocity dependence of friction mediated by dynamics of interfacial contacts, *Physical Review Letters* **123**, 116102 (2019).
- [20] Y. Liu and I. Szlufarska, Chemical origins of frictional aging, *Physical Review Letters* **109**, 1 (2012).
- [21] A. Filippov, J. Klafter, and M. Urbakh, Friction through dynamical formation and rupture of molecular bonds, *Physical Review Letters* **92**, 1 (2004).
- [22] Z. Li and I. Szlufarska, Chemical creep and its effect on contact aging, *ACS Materials Letters* **4**, 1368 (2022).
- [23] L. Peng, C. Hsu, C. Xiao, D. Bonn, and B. Weber, Controlling macroscopic friction through interfacial siloxane bonding, *Physical Review Letters* **131**, 226201 (2023).
- [24] C. Leriche, C. Xiao, S. Franklin, and B. Weber, From atomic attrition to mild wear at multi-asperity interfaces: The wear of hard Si_3N_4 repeatedly contacted against soft Si, *Wear* **528**, 204975 (2023).
- [25] T. H. Goebel, E. E. Brodsky, and G. Dresen, Fault roughness promotes earthquake-like aftershock clustering in the lab, *Geophysical Research Letters* **50**, e2022GL101241 (2023).
- [26] C. Hsu, F. Hsia, B. Weber, M. De Rooij, D. Bonn, and A. Brouwer, Local shearing force measurement during frictional sliding using fluorogenic mechanophores, *The Journal of Physical Chemistry Letters* **13**, 8840 (2022).
- [27] S. M. Rubinstein, G. Cohen, and J. Fineberg, Detachment fronts and the onset of dynamic friction, *Nature* **430**, 1005 (2004).
- [28] O. Ben-David, S. M. Rubinstein, and J. Fineberg, Slip-stick and the evolution of frictional strength, *Nature* **463**, 76 (2010).
- [29] D. S. Kammer, V. A. Yastrebov, P. Spijker, and J.-F. Molinari, On the propagation of slip fronts at frictional interfaces, *Tribology Letters* **48**, 27 (2012).
- [30] Z. Li, L. Pastewka, and I. Szlufarska, Chemical aging of large-scale randomly rough frictional contacts, *Physical Review E* **98**, 1 (2018).
- [31] C. Leriche, C. Xiao, S. Franklin, and B. Weber, From atomic attrition to mild wear at multi-asperity interfaces: The wear of hard Si_3N_4 repeatedly contacted against soft Si, *Wear* **528-529**, 204975 (2023).
- [32] O. Ben-David, S. Rubinstein, and J. Fineberg, Slip-stick and the evolution of frictional strength, *Nature* **463**, 76 (2010).
- [33] B. Weber, T. Suhina, T. Junge, L. Pastewka, A. Brouwer, and D. Bonn, Molecular probes reveal deviations from amontons' law in multi-asperity frictional contacts, *Nature Communications* **9**, 1 (2018).
- [34] V. Romero, E. Wandersman, G. Debrégeas, and A. Prevost, Probing locally the onset of slippage at a model multicontact interface, *Physical Review Letters* **112**, 1 (2014).
- [35] P. Berthoud, T. Baumberger, C. G'sell, and J.-M. Hiver, Physical analysis of the state-and rate-dependent friction law: Static friction, *Physical review B* **59**, 14313 (1999).
- [36] T. Baumberger and C. Caroli, Solid friction from stick-slip down to pinning and aging, *Advances in Physics* **55**, 279 (2006).
- [37] R. Capozza and M. Urbakh, Static friction and the dynamics of interfacial rupture, *Physical Review B—Condensed Matter and Materials Physics* **86**, 085430

- (2012).
- [38] L. Frérot, G. Anciaux, V. Rey, S. Pham-Ba, and J.-F. Molinari, Tamaas: a library for elastic-plastic contact of periodic rough surfaces, *Journal of Open Source Software* **5**, 2121 (2020).
 - [39] F.-C. Hsia, C.-C. Hsu, L. Peng, F. M. Elam, C. Xiao, S. Franklin, D. Bonn, and B. Weber, Contribution of capillary adhesion to friction at macroscopic solid–solid interfaces, *Physical Review Applied* **17**, 034034 (2022).
 - [40] S. Pradhan, A. Hansen, and B. K. Chakrabarti, Failure processes in elastic fiber bundles, *Reviews of Modern Physics* **82**, 499 (2010), publisher: American Physical Society.

SUPPLEMENTAL MATERIAL

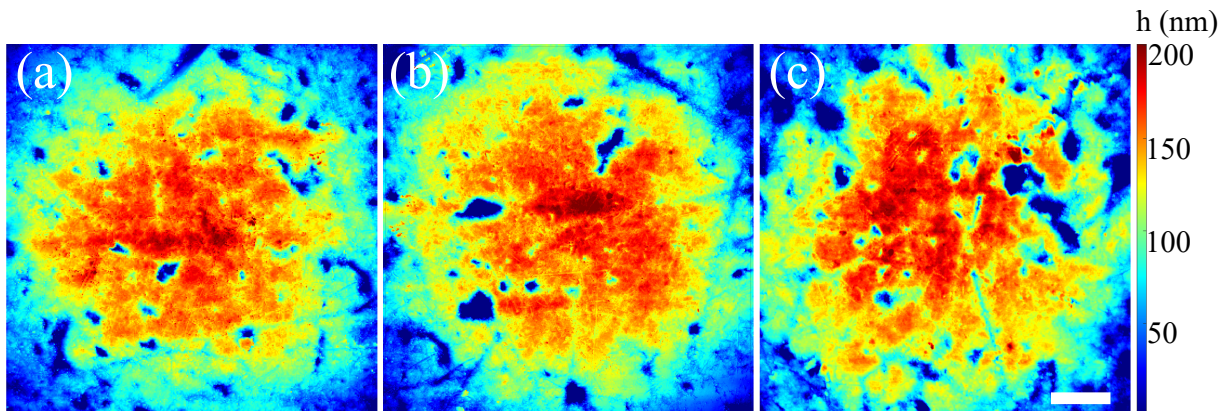


FIG. S1. AFM topography. (a)(b)(c) Three different AFM topographies measured from silicon balls used in experiments. Measurements were taken using tapping mode in AFM (Dimension Icon, Bruker) with Si tips (RTESPA-300, Bruker). The topography size is $31.13 \times 31.13 \mu\text{m}^2$ with a RMS (root-mean-square) roughness around 40 nm. Scale bar, 5 μm .

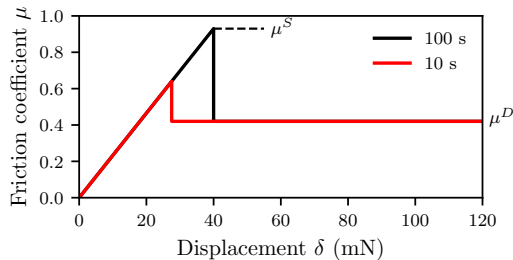


FIG. S2. Nanoscale friction coefficient-displacement curve used for simulation in Fig. 2. The black and red curves correspond to the AFM SHS measurements for a hold time of 100 s and 10 s, respectively. The static and dynamic friction values for a hold time of 100 s are indicated respectively with μ^S and μ^D .

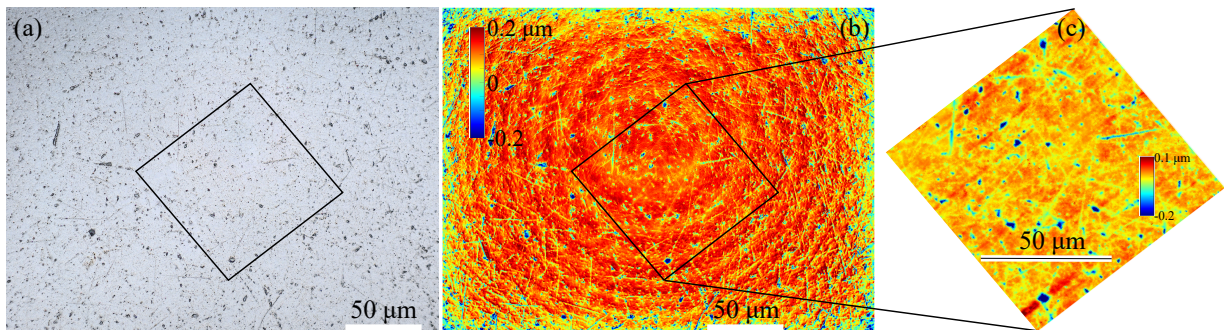


FIG. S3. Topography of silicon ball apex after friction experiments. (a) Optical image of the apex of silicon ball captured over an area of $283 \times 212 \mu\text{m}^2$, using a laser-scanning confocal profilometer (Keyence VK-X1000). (b) Height profile derived from the optical image in (a). (c) AFM topography with a size of $90 \times 90 \mu\text{m}^2$, which corresponds to the square-marked area in (a) and (c). Both optical and AFM images reveal no visible signs of wear, indicating minimal impacts of wear on our experimental result. Scale bar, 50 μm .

Supplemental movies

Three supplemental movies are associated with this manuscript:

- “SupplementalMovie01mN.mp4”, focusing on a normal load $N = 0.1$ mN.
- “SupplementalMovie1mN.mp4”, focusing on a normal load $N = 1$ mN.
- “SupplementalMovie10mN.mp4”, focusing on a normal load $N = 10$ mN.

Each movie shows the evolution of the distribution of local friction coefficients with increasing imposed displacement, with the critical asperities ($\mu = \mu^S$) in brown, the pre-sliding asperities ($\mu = \mu^D$) in yellow, and the subcritical asperities ($\mu < \mu^0$) in green. The movies are available [online](#).